Journal of Materials Chemistry B

ROYAL SOCIETY OF CHEMISTRY

PAPER

View Article Online
View Journal | View Issue

Cite this: *J. Mater. Chem. B*, 2025, **13**, 6755

Raman microscopy as a tool to study changes in chemical composition upon structural differentiation of *Ambystoma* embryo†

Victor V. Volkov and Carole C. Perry *

Received 19th December 2024,
Accepted 30th April 2025

DOI: 10.1039/d4tb02808b

rsc.li/materials-b

Ambystoma mexicanum is often used in regeneration studies because it reaches sexual maturity as aquatic larvae within 360 hours, and it can regenerate its appendages. In developing a spectroscopic approach for regeneration studies, in this contribution, we show that Raman confocal microscopy can be used as a diagnostic tool to describe the chemical composition of axolotl embryonal tissues at different stages of development. Experimental observations, supported by quantum chemistry studies on molecules reported or considered to be present in the tissues of the living organism, show that in the early stages of development (Harrison stage 11), there is only limited spatial differentiation of phospholipid, carotenoids and proteins, though, in the later stages of development (Harrison stage 33), differentiation of chemical species is possible and can be related to the development of tissues and organs. In particular, we were able to assess the oxidation state of proteins, their packing and the role of pigments in protection of cellular tissues. We believe the results presented here will be helpful for those involved in planning experiments to combine biochemistry, emission and Raman microscopy to research axolotl tissue regeneration mechanisms.

Introduction

In contrast to salamanders, which undergo metamorphosis to a terrestrial form, the Mexican axolotl (*Ambystoma mexicanum*) reaches sexual maturity in its aquatic larvae.[1] Introductory developmental studies described 49 development stages of an axolotl embryo.[2] At 20 °C *Ambystoma mexicanum* takes 360 hours to grow and transform into a mature animal[3] which makes axolotl attractive for laboratory studies. Indeed, early publications reported the animal as practical and helpful for transplantation studies.[4,5] Later, axolotl was recognized as a highly regenerative model organism – one of the few adult vertebrate species capable of complete regeneration of missing body parts throughout life.[6] This unique capacity has generated several hypotheses: axolotls may not complete metamorphosis and their cells retain some embryonic-like characteristics,[7] or this behaviour may correlate, possibly, with their depleted immunity and inflammatory response.[8,9] Aspects of the cellular and molecular mechanisms of axolotl regeneration are being researched including signalling from a wounded tissue, formation of a blastema (a limb bud-like mass of dedifferentiated mesenchymal progenitors) and recovery of injured nerves and connective tissue cells.[10–13]

Clarification of regeneration processes may require combining genetic insight (for example, on transcripts that define progenitors of tissues along the temporal path of regeneration[14]) with the recovering tissue restructuring after surgical intervention.[15] In this process, monitoring chemical signatures of structural rearrangements at the sub-micron level may support understanding the molecular mechanisms involved. Raman spectral sampling is an approach that allows label-free specification of chemical species under sub-micron resolution. For example, nonlinear coherent Raman microscopy (CARS) was reported to describe myelin fragmentation and recovery upon and after damage of an axolotl nerve.[16]

As an alternative to nonlinear Raman spectroscopy, which is sensitive to phase-matching conditions, spatial anisotropy and wavelength specific non-resonant and resonant contributions,[17] conventional (incoherent, spontaneous) Raman confocal microscopy can also be used as it has the capacity to be quantitative on molecules present and their orientation.[18] As an example, conventional Raman spectroscopy has been used to describe the chemical composition of Xenopus frog,[19] ovine,[20] and mouse[21,22] embryonal tissues. Additionally, Raman spectroscopy has been used for effective hyperspectral mapping of different chemical species in bovine oocyte[23] and zebrafish larvae.[24] Furthermore, Raman microscopy was performed in the confocal regime to

Interdisciplinary Biomedical Research Centre, School of Science and Technology, Nottingham Trent University, Clifton Lane, Nottingham NG11 8NS, UK.
E-mail: carole.perry@ntu.ac.uk

† Electronic supplementary information (ESI) available. See DOI: https://doi.org/10.1039/d4tb02808b

pioneer hyperspectral 3D tomography of a complete zebrafish embryo.[25]

Oocytes and zebra fish larvae are the species on which most research has been conducted. On the one hand, they demonstrate an important plethora of developmental biochemistry; on the other hand, their structural and optical properties provide relatively easy sampling when using optical microscopy. Due to the higher level of dense structuring, microscopy sampling of amphibian, avian and mammal embryonal tissues is a different level of challenge.

In this study, we conduct confocal Raman microscopy on tissues of axolotl embryos at stages 11 and 33; in the former embryo, lateral lips have formed making the blastopore into a semicircle, while for the latter we deal with a larva with a clear tail and head as well as responsive body muscles.[3] The two selected stages provide opportunities to explore the different molecular compositions and distributions in embryonal space when an organism is at the beginning and nearly the end of its formation. The second stage is intermediate on the path of organism development. This is where appendages and sensorial organs in introductory form are becoming apparent. Exploring axolotl early eye formation may provide a development model platform for ocular biochemistry, pathology and regeneration studies.[26–28] The same concerns opportunities to monitor the biochemistry of growth and recovery of body constituent components and projectiles.[15,29,30]

To aid molecular analysis, we conduct quantum chemistry studies to generate Raman tensors for molecules which are reported or considered to be present in constituent tissues of axolotl. To the best of our knowledge, the spatial description of molecular species of axolotl tissues at different stages of development is reported for the first time. This is the first stage in a plan to see if confocal Raman microscopy is suitable to address regenerative mechanisms in the axolotl model.

Materials and methods

Sample preparation

Home produced axolotl eggs and larvae were kept at 24 °C. Studies were carried out in accordance with recommendations in the Guide for the Care and Use of Laboratory Animals of the National Research Council;[31] first, organisms were anaesthetized in 0.1% ethyl 3-aminobenzoate (#E10521; Sigma, St. Louis, MO, USA), then were euthanized by tricaine overdose.

Specimens for microscopy studies were embedded in cavities cut into polytetrafluoroethylene membranes deposited on an unprotected gold coated 12.7 × 12.7 × 0.6 mm mirror PFSQ05-03-M03 from Thorlabs Ltd. The gold coated mirrors are chemically inert, while the highly smooth metallic layer ensures that the substrate does not contribute to either the Raman or emission signals. The mirror with a specimen was fixed in a 35 mm diameter Petri dish from Thermo Scientific™ Sterilin™ to provide an aqueous environment for the specimens *via* channels to the fixing cavities. All measurements were conducted at room temperature (24 °C). Specifically, we scanned (i) a structural element of an early blastopore lateral lip; (ii) epidermic precursors of the cornea of an embryo at Harrison stage 33; and (iii) the tip of its tail, as we demonstrate in Fig. 1, left side. The first specimen was scanned with a step of 1 micron along both directions, while the other larger samples were measured using a step of 10 microns along both directions.

Raman microscopy instrumentation

Spectrally resolved Raman microscopy studies were conducted using a DXR microscope from Thermo Fisher Scientific, Madison, Wisconsin, equipped with 100× microscopy objective with numerical aperture 0.8, and using 532 nm excitation radiation. The radiation power was set to 2 mW, according to the

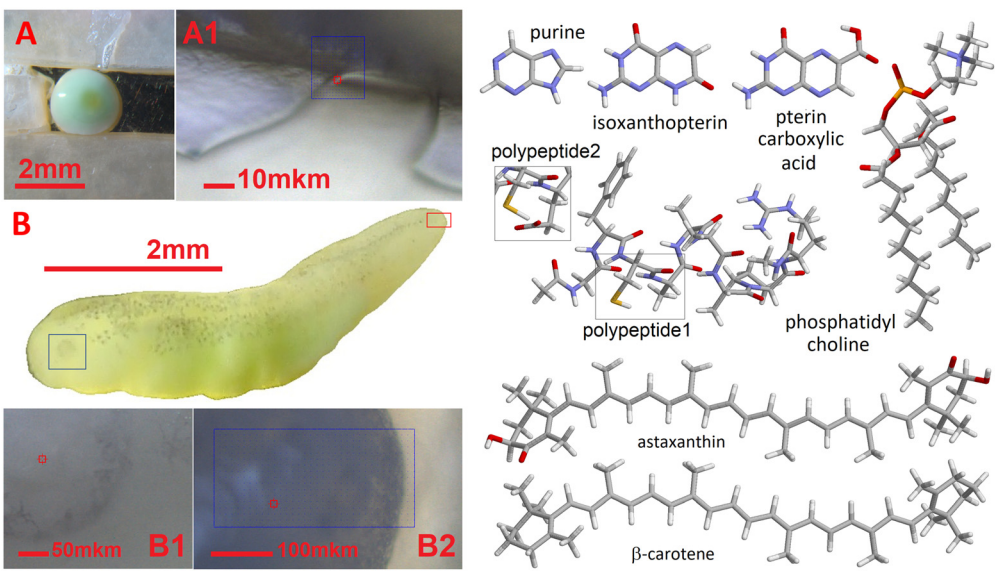

Fig. 1 Left: Bright field optical microscopy images of an early blastopore, Harrison stage 11 (A) and of a structural element of its lateral lip (A1); of Harrison stage 33 axolotl embryo (B), its eye (B1); and at the tip of its tail (B2). Boxed fields indicate the areas where we conduct confocal Raman scanning. Right: Model molecular systems.

microscope internal diagnostics. Under the adopted focusing conditions, the selected excitation power was tested in advance not to induce physical nor thermal-physical damage of the selected type of specimens: the ocular samples were the most sensitive. The spectral resolution of scanned images was 2 cm^{-1}, according to the instrumental limit of the microscope operated using a 25 micron confocal pinhole. Calibration of the instrument was according to the manufacturer's procedures.

Raman image reconstruction protocol

Spectra sampled at different sites, i, were fitted to extract the intensity of Raman activities, $A_{\omega,i}$, at frequencies of interest, ω, which were used in reconstructions of Raman microscopy images (RAM).[32] To visualize microscopy images specific to selected Raman activities (RAM) we map Raman signals in the image plane according to RAM $(X, Y, \omega) = \sum_i \left(A_{\omega,i}/2\pi\sigma^2\right) \exp\left[-(X - X_i)^2/2\sigma_x^2\right]\exp\left[-(Y - Y_i)^2/2\sigma_y^2\right]$. Here i is the index of a site where a spectrum is taken, $A_{\omega,i}$, is the amplitude of intensity of a Raman resonance of interest in the detected spectra, and ω is the frequency of the resonance. X_i and Y_i describe the position of the projection of the site i into the image plane. X and Y variables are sample distances from the site i in terms of the dimensions of detector pixels or displacements of a pinhole. An image is reconstructed taking the sum of projections of two-dimensional Gaussian source functions over the defined sites i. When the scanning step size is 1 micron, the spatial full width of a source function setting $\sigma_x^2 = \sigma_y^2 = 0.6$ μm^2: this reflects the dimensions of the emitting coherent envelope, using 532 nm excitation radiation. To reconstruct images scanned using 10 microns steps, the source function was 6 μm^2 to provide a smooth image interpolation.

Molecular model systems

To discuss the experimental results, Raman tensors for several representative model molecular systems were calculated. For example, to address spectral contributions of phospholipids, we computed Raman spectra of 1,2-didecanoyl-*sn-glycero*-3-phosphatidylcholine and 1,2-didecanoyl-*sn-glycero*-3-phosphatidylinositol. Fig. 1 right side presents a structure of the phosphatidylcholine molecule. The adopted phospholipid molecules are helpful to model types of vibration and frequencies to be expected in lipid membranes. At the same time, in such systems collective phenomena are reported to affect intensities, broadenings and slight spectral shifts. These are discussed based on results of previously reported experiments.[33–35]

In the case of a protein model, we adopted the 582–592 (LDIVKLLLPRG) span of ankyrin helical fold according to 1n11.pdb entry,[36] which was modified to polypeptide 1 (Met-GFCAAAAPRMet) and polypeptide 2 (Met-GFCEAAAPR-Met) model systems. Since we are interested in reproducing protein spectral signatures, we methylate both sides to avoid polar variances at the terminals and to mimic hybridization of Cα atoms of the terminal peptides. Both, proline and arginine are in the original sequence as they contribute significantly to the native secondary structure. Introduction of phenylalanine instead of isoleucine allows modelling the Raman signature of the aromatic moiety. To reduce polar variance next to the terminal and to reduce the number of atoms, we replace aspartic acid with glycine and leucine residues with alanine, respectively. In order to compute Raman properties of a cysteine residue side group, while accounting possible variance of degree of hydrogen bonding,[37] in polypeptide 1 we replace native valine and lysine with cysteine and alanine, whereas in polypeptide 2, we replace native valine and lysine with cysteine and glutamic acid; to obtain further details, see images of the structures in the right side of Fig. 1. In polypeptide 1, the SH moiety is in a relatively hydrophobic environment, while in polypeptide 2, the moiety is effectively hydrogen bonded to the COO group of the next residue.

Wild axolotls are pigmented: there are three types of pigment cells: melanophores, xanthophores, and iridophores. Melanophores contain brown eumelanins, iridophores purines, and xanthophores pteridines.[38,39] The content, distribution and arrangement of pigment cells change during axolotl development: melanophores and xanthophores appear early in development, and iridophores are present somewhat later.[40] In our studies, we explore the properties of axolotl albino form. The albino gene was introduced by hybridization (*via* artificial insemination) between a female albino *Ambystoma tigrinum* and white *Ambystoma mexicanum* males.[41] Albino axolotls are not just amelanotic versions of the wild-type; it is considered that their (overall) bright yellow coloration and shiny areas in albino skin are presumably due to pteridines and iridophores, respectively. Since thin-layer chromatographic separation of ethanol-extracted pteridine pigments from larval and adult stage axolotl skin suggested the presence of purine, guanine, pterin, isoxanthopterin, xanthopterin, pterin-6-carboxylic acid, biopterin, sepiapterin, erythroneopterin and riboflavin[40,42] we computed Raman spectra for these chromophores. Fig. 1 right side presents structures for the selected chromophores. ESI† provides the full data set.

Another group of expected pigments are carotenoids as they play an important protective role in antioxidant defence systems.[43] Since carotenoids are lipophilic molecules, they are typically found in skin,[44] in the retina and yolk of vertebrates.[45,46] The presence of β-carotene was reported in *Xenopus laevis* oocytes.[19] Taking carotenoid biochemistry and their structural diversity into account,[47] in this contribution, we compute the properties of astaxanthin and β-carotene; for details, see structures in the right side of Fig. 1.

Density functional theory

Optimization and normal mode analysis are performed using the 6-31++g(d,p) basis set and the restricted B3LYP hybrid functional[48,49] as implemented in the Gaussian 09 program package.[50] To account for the proximity of the experimental excitation wavelength (532 nm) to molecular electronic resonances, we compute pre-resonant Raman intensities using frequency-dependent (dynamic) coupled-perturbed Hartree–Fock equations, which are specific to the incident light frequency for the electromagnetic field perturbation according to Gaussian 09 option cphf = rdfreq.[50] To plot Raman spectral dispersions according to DFT predictions, we adopt a frequency

scaling factor of 0.97, and we compute convolutions using Lorentzian line-shapes with a full width at half maximum of 8 cm^{-1}.

Results and discussion

To address the diversity of chemical species we may assess during the early development of axolotl embryonal tissues using label free Raman diagnostics in Fig. 2A–C, we compare representative spectra averaged using microscopy resolved sampling over selected structural elements of the blastopore lateral lip, early eye specimen and tip tail of the embryo, as shown in Fig. 1A1, B1 and B2, respectively. The reported range of spectral signatures reflects the complexity of the transforming organism, which recapitulates the accumulated content of the evolution of the organism: according to the Meckel–Serres conception, the embryo recapitulates stages, which resemble successive adult stages in the evolution of the animal's remote ancestors.[51,52]

We suggest assignments of Raman activities starting from quantum chemistry predictions for typical and/or plausible molecular archetypes: Fig. 2D–F show Raman spectra computed for phosphatidylcholine, helical polypeptides modelled as described in the Materials and methods section, and selected pteridine pigments and carotenoids, respectively. ESI† contains computed data for the full set of the considered molecules. According to the results of quantum chemistry we suggest assignments for amide and phenylalanine specific modes of proteins, delocalized stretching modes of carotenoids, representative signatures of phospholipids and plausible Raman contributions due to pteridine pigments; please, see the corresponding notations in Fig. 2A–C.

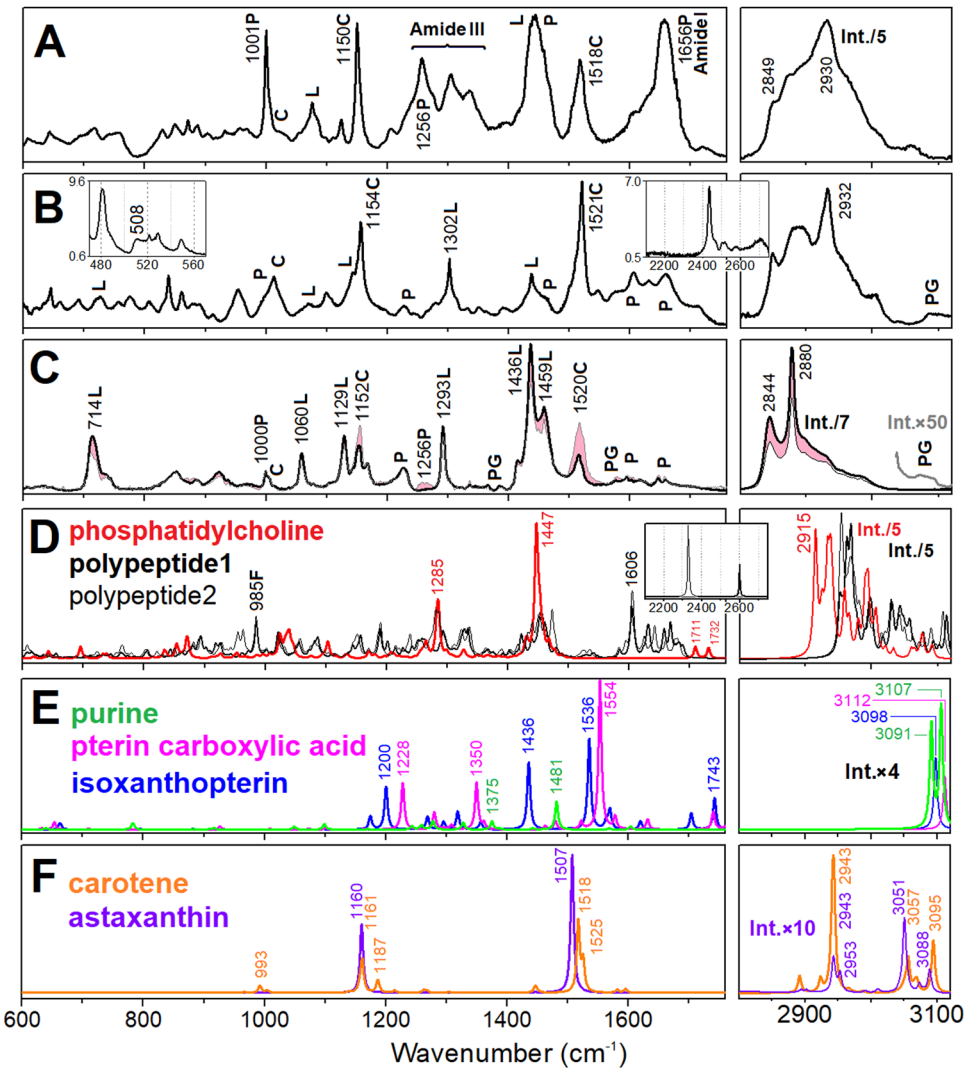

Fig. 2 Representative Raman spectra taken at the structural element of the blastopore lateral lip (A), at the side of the eye and its cornea (B); and at the tip of the tail (C) sampled in the scanned area as shown in the left set of Fig. 1. To understand the diversity of chemical species sampled in the relatively large scanned area, in panel C, we color spectral regions of large intensity variance. (D)–(F) Raman spectra computed for the model molecular systems, as shown in the right side of Fig. 1. Labels P, L, C and PG indicate Raman resonances, which we assigned to proteins, phospholipids, carotenoids and pigments, respectively. To plot computed Raman spectra, we adopt a frequency scaling factor of 0.97, and convolutions with Lorentzian line-shape with full width at half maximum of 8 cm^{-1}.

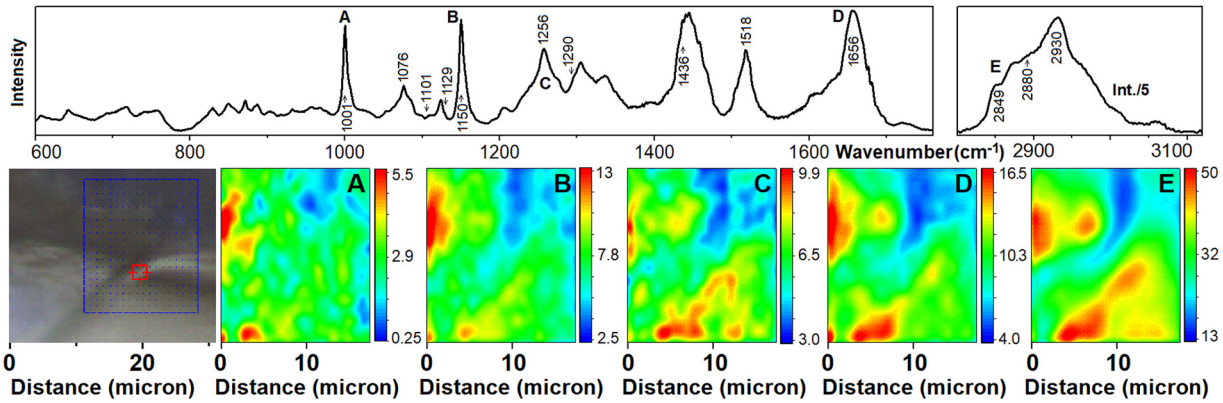

Fig. 3 Raman micro-spectroscopy of the axolotl blastopore. Upper panel presents the corresponding average spectrum as shown in Fig. 2. Images are reconstructed using Raman signals at 1001 cm^{-1} of phenylalanine side group (A), at 1152 cm^{-1} of carotenes (B); at 1260 cm^{-1} and 1653 cm^{-1} of protein amide III and I (C and D, respectively); at 2850 cm^{-1} what is specific to CH stretching modes of phospholipids, mainly (E). Labels of Raman resonances in the upper panel correspond to notations of panels with Raman microscopy images reconstructed at the corresponding frequencies.

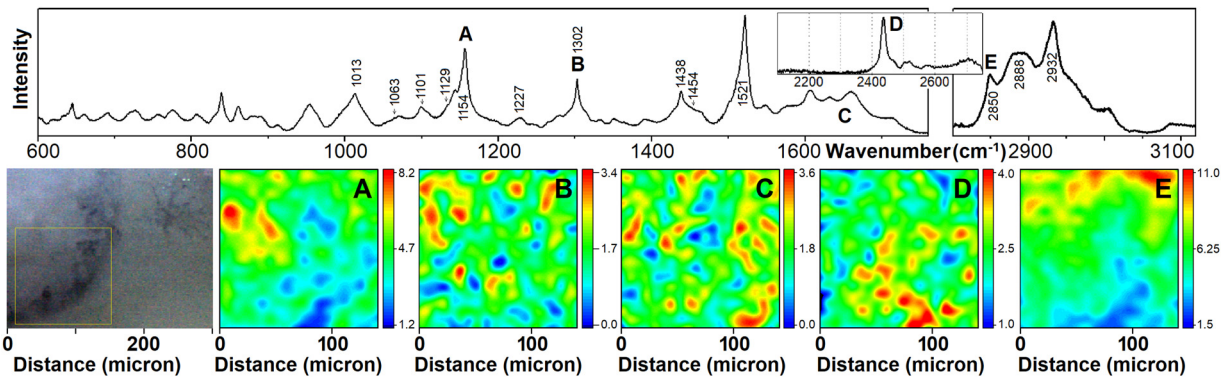

Fig. 4 Raman micro-spectroscopy of the axolotl embryo ocular sample. The upper panel presents the corresponding average spectrum as shown in Fig. 2. (A)–(E) Images reconstructed using Raman signals at 1154 cm^{-1} (carotenes), 1302 cm^{-1} (phospholipids), 1630 cm^{-1} (protein amide I), 2460 cm^{-1} (cysteine S–H stretching), and 2850 cm^{-1} (CH stretching modes of phospholipids, mainly) as detected in the boxed area of the axolotl embryo eye, as shown in the left side bright optical microcopy image or in Fig. 1B1. Labels of Raman resonances in the upper panel correspond to notations of panels with Raman microscopy images reconstructed at the corresponding frequencies.

Adopting the assignments, in Fig. 3–5, we present microscopy images of the selected area of the embryonal tissues reconstructed using Raman intensities at frequencies as indicated. In the following, we provide detailed descriptions of chemical compositions for each of the cases. The descriptions suggest a tentative guide on what can be observed in the axolotl embryonal tissues using Raman diagnostics. Accordingly, accounting for the nature of the stages, we address the biochemistry and the possibility to map changes in biochemistry as instructed by embryonal development.

Blastopore lateral lip sample

Let us start with Raman characteristics of the early blastopore as shown in Fig. 1A1. First, we consider the main cellular components, proteins and lipids. The representative Raman spectrum (see Fig. 2A) shows spectrally broad bands at 1653 and 1436 cm^{-1} and spectrally narrow resonances at 1150 and 1518 cm^{-1}. The band at 1653 cm^{-1} is due to amide I of proteins, where α-helical components dominate. Furthermore, clear spectral signatures of amide III vibrations are observed in the spectral region 1220–1340 cm^{-1}. According to results published previously[53] and consistent with our DFT studies, at the lower frequency side of the band at 1436 cm^{-1} arise from phospholipid CH_2 scissor modes (of different degrees of delocalization) specific to hydrocarbon tails, choline and glycerol moieties. Consistent with our DFT results (see computed spectra in Fig. 2D) and the Raman signature of skin macromolecular components,[54] we assign the higher frequency side spectral broadening of the band to CH_3 wags and CH_2 scissor modes of proteins.

In the higher frequency spectral range, the spectrally broad contribution at 2880 cm^{-1} and the band at 2849 cm^{-1} correspond to antisymmetric and symmetric CH_2 stretching vibrations, respectively.[55] Both, the spectrally unresolved character of these signatures and low I_{2880}/I_{2849} ratio suggest diminished lateral packing density and a lack of order for phospholipids in this protein rich sample.[53] Considering the spectral width of the antisymmetric stretching band, we cannot exclude a contribution of hexagonal molecular arrangements,[55] as previously reported for tissues from the stratum corneum.[56] We may ascribe the relatively broad dominant band at 2930 cm^{-1} to both protein and

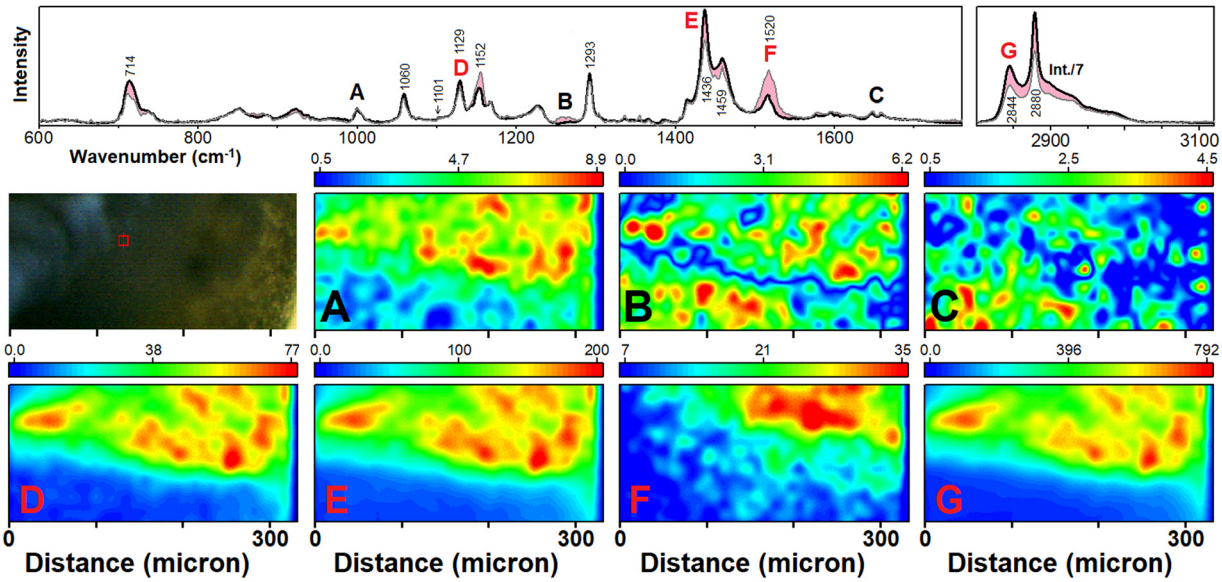

Fig. 5 Raman micro-spectroscopy of the axolotl embryo caudal appendage sample. Upper panel presents the corresponding average spectrum as shown in Fig. 2. (A)–(C) Images reconstructed using Raman signals at 1001 cm^{-1} (phenylalanine), 1265 cm^{-1} (amide III), and 1650 cm^{-1} (amide I) as detected in the boxed area of the axolotl embryo tail, as shown in the left side bright optical microcopy image or in Fig. 1B2. (D)–(G) Images reconstructed using Raman signals at 1129 (phospholipids), 1436 (phospholipids), 1520 (carotene) and 2844 cm^{-1} (phospholipids) as detected in the same area. Labels of Raman resonances in the upper panel correspond to notations of panels with Raman microscopy images reconstructed at the corresponding frequencies.

carotenoid contributions. This agrees with the results of DFT studies as shown in Fig. 2D and F.

Comparing our data to the literature, it is interesting to note that the representative Raman spectrum from the cytoplasm of an oocyte of *Xenopus laevis* demonstrated a relatively small amount of protein, where the α-helical component was not dominant.[19] However, the comparative contributions of lipid and proteins as well as the prevalence of α-helical components (as we detect) correspond well to those reported in Raman studies of a 2,4,8-celled mouse embryo.[57] The authors discussed that switching from the production of β-sheet rich proteins to α-helical proteins is a signature of genetic activation after fertilization.

Next, let us consider the presence of pigments. We ascribe two spectrally sharp resonances at 1150 and 1518 cm^{-1} to carotenoids. The resonances are similar to the pre-resonant spectra computed for astaxanthin and β-carotene (see Fig. 2F). Such chromophores are reported in the yolk of vertebrates.[45] Furthermore, the presence of β-carotene has been previously reported in *Xenopus laevis* oocytes.[19]

Having general assignments, in Fig. 3, we compare spatial distributions of carotenes (1150 cm^{-1}), lipids (2850 cm^{-1}) and proteins (1001, 1260 and 1650 cm^{-1}). The reconstructed maps are quite similar, which may correspond to a relatively weak degree of functional differentiation of the selected stage of embryonal development. Also, it is interesting to note the relatively rich contribution of carotenoids, which are co-present with proteins and lipids. Indeed, carotenoids are the source of retinoic acid that binds the nuclear retinoic acid receptors to regulate the transcription of hundreds of genes that are critical for early embryogenesis.[58]

Ocular sample

The bright field microscopy image at the left side of Fig. 4 shows a selected region of the ocular specimen of the embryo at Harrison stage 33. According to Cuny and Malacinski,[59] at this stage, the initial pair of optic vesicles demonstrate a significant transformation. Specifically, the vesicles expand, and their walls (facing the head epidermis) are thickened to form a neural retina, which subsequently becomes a concave lens hemisphere; a planar lens placode (formed by the thickened internal layer of the head epidermis) contracts to form the lens hemisphere. The bright field microscopy image at the left side of Fig. 4 (and in Fig. 1B1) demonstrates the lens hemisphere structure covered with an epidermal precursor of the sclera. The image shows local dark fibrillar spots, which may suggest extra thick structuring with possible pigment depositions.

The representative Raman spectrum (Fig. 2B) for the sample includes resonances at *ca.* 1302 and 1420 cm^{-1}. Following the results of our DFT studies and literature,[53,60] we ascribe the vibrations at 1302 cm^{-1} to CH_2 twists of phospholipids mainly and proteins marginally (see Fig. 2D). In the mid-IR spectral region, the Raman spectrum includes amide I transitions, suggesting a moderate presence of proteins while the signal from largely helical structural components (at 1650 cm^{-1}) is no longer dominant, as found for the early blastopore.

There are prominent resonant Raman peaks at 1154 and 1521 cm^{-1}, which are characteristic of carotenoids. The peaks originate, respectively, from the C–C single-bond and the C=C double-bond stretching vibrations of the molecule's conjugated carbon backbone, while the weaker peak at 1013 cm^{-1} is attributed to the rocking motion of the molecule's methyl side groups.[61]

Carotenoid molecules play an important protective role in the skin's antioxidant defence system.[62] If unbalanced due to a lack of antioxidants, the destructive effects of reactive oxygen species and free radicals can lead to skin malignancies and disease. In animal models, carotenoids have been shown to inhibit carcinoma formation in the skin.[63] According to DFT predictions for astaxanthin and β-carotene (see Fig. 2F) we anticipate the sharp peak at 2932 cm^{-1} to be a signature of carotenoids, as well.

As we addressed in the Materials and methods section, the results of chromatographic studies indicated that albino axolotl skin contains pteridine pigments.[40,42] According to our DFT predictions (see Fig. 2E), the weak Raman signals at 1590 and 3100 cm^{-1} may suggest a small amount of such pigments in the epidermis of the head and in the epidermis of the ocular region, in particular.

In the wavenumber range between 2400 and 2600 cm^{-1}, the spectrum detected for the ocular sample reports a dominant peak at 2436 cm^{-1} and several weak resonances at 2467, 2502, 2518 and 2574 cm^{-1}. Early Raman studies on bovine[64] ocular lens proposed that reduced SH moieties of proteins contribute to this spectral region. In particular, Raman resonances at 2558 cm^{-1} and the shoulder near 2560 cm^{-1} as detected in bovine lens (in the nucleus and in the cortex) were ascribed to two distinct environments for SH groups. Later, the relative presence of reduced SH moieties under different degrees of hydration was discussed in relation to physiological conditions and aging.[65,66] The main Raman resonance we detect is at a lower frequency than reported for bovine samples. This may suggest both, a better hydrated environment and different protein biochemistry of amphibian development. The results of our DFT studies for the SH vibration in polypeptides where the moiety is under effective hydrogen bonding to a neighboring glutamic acid (polypeptide 2) or embedded in a relative hydrophobic environment by proximal methyl groups (polypeptide 1) indicate a sufficiently wide spectral range to support the observed frequency according to the degree of polar interaction with near neighbours and the environment. This agrees with the spectral variances anticipated for the SH vibration of the amino acid cysteine when paired with different proton containing molecules.[67]

It is interesting that the status of protein oxidation can be accessed using the ratio of SS (508 cm^{-1}) and SH (2580 cm^{-1}) modes.[68–70] As the Raman signature we detect at 508 cm^{-1} (see left insert in Fig. 2B) is about 6.5 times weaker than the peak at 2436 cm^{-1}, we may note dominance of the reduced state of the protein which may be important for structural flexibility upon embryonal development.

We now compare spatial distributions of carotenes (1154 cm^{-1}), lipids (1302 and 2850 cm^{-1}) and proteins (1630 and 2460 cm^{-1}). In contrast to the distributions detected for the blastopore, panels of Raman patterns (as shown in Fig. 4) demonstrate two scenarios. The weaker signal of phospholipid at 1302 cm^{-1} (Fig. 4B) tends to agree with the spatial distribution reconstructed at 2850 cm^{-1} (Fig. 4E). In the lower region of the corneal limbus there is a lack of phospholipid Raman intensity. Instead, the phospholipid contribution becomes more prominent toward the centre of the eye. The distribution of carotenoids (Fig. 4A) follows the presence of phospholipid. This corresponds to the lipophilic nature of the chromophore. In contrast, maps for amide one and for SH vibration indicate the dominance of proteins in regions of lower phospholipid content. This may be an indication of protein machinery localisation to provide further growth and restructuring.

Similar to the previous sample, spectrally broad bands at 2850 and 2888 cm^{-1} show a rather low I_{2880}/I_{2849} ratio which suggests a decreased lateral packing density and a lack of order for phospholipid tails.[53] This agrees with the comparable intensities for skeletal C–C stretchings at 1129 and 1101 cm^{-1}. This suggests the role of *gauche* isomers which dominate in a liquid crystalline phase.[33]

Caudal appendage sample

Finally, we consider the capacity of Raman spectroscopy and microscopy to resolve molecular distributions within a semi-transparent region of the body tail tip; see bright field microscopy images in Fig. 1B2 and expanded view in Fig. 5. To approach spectral properties, we must consider the tissue composition we scan. In this instance, this concerns the skin: *Ambystoma* skin has both epidermis and dermis. The epidermis of adult axolotls consists of several cell layers containing non-keratinised cells, basal cells and Leydig secreting cells.[71] Already before hatching, Leydig cells were reported between the two epidermal cell layers, which are characteristic for this stage.[72] The dermis holds mucous and granular glands within the stratum spongiosum – a network of collagen fibres above the stratum compactum, which forms a compressed collagen layer on top of the hypodermis to separate skin from the underlying muscle.[73] Collagen is the key matrix to preserve elasticity and firmness.[74]

In Fig. 2C, we present representative Raman spectra to account for the main spectral features and intensity variances for the region of the microscopy study. Raman spectral components of phospholipids dominate. The spectrally narrow character of phospholipid resonances at 1436, 1459, 2844, and 2880 cm^{-1} signify that the alkyl chains are in tight and relatively ordered lattices.[55] A relatively high intensity ratio $I_{2880}/I_{2844} \approx 2.1$ suggests an elevated lateral packing density.[53] This agrees with the skeletal C–C stretching ratio $I_{1129}/I_{1101} > 2$ indicating that all-trans isomers dominate.[33] The prominent resonance at 714 cm^{-1} is due to the stretching vibrations of phospholipid C–N bonds.[75] If such is the case, since relatively localized, under polarisation conditions, this scattering may serve as a valuable surface structural marker.

In the spectral range of the amide I band, Raman spectra show two weak bands at 1647 and 1659 cm^{-1}. The former resonance is due to the alpha-helical component and the latter Raman signal is ascribed to collagen;[75] in particular, it is instructive that while collagen fibers demonstrate an amide I band at 1671 cm^{-1}, a collagen signal from skin normal dermis is reported at 1659 cm^{-1}.[76] Raman resonances at 1154 and 1520 cm^{-1} are indicative of the presence of carotenoids, while relatively weak Raman scattering at 1590 and 3090 cm^{-1} may suggest small contributions of pteridine pigments.

Having Raman microscopy maps reconstructed for different frequencies, in Fig. 5 we group them into two sets according to spatial patterns. Specifically, Fig. 5A–C demonstrate Raman scattering distributions for resonances of phenylalanine (at 1001 cm^{-1}), amide III (at 1265 cm^{-1}) and amide I (signal is summed within 1630–1670 cm^{-1} spectral region), respectively. In all cases, Raman scattering fills the full image space. In Fig. 5D, E and G we present Raman maps for resonances of phospholipids at 1129, 1436 and 2844 cm^{-1}, respectively, while in Fig. 5F, we show the spatial distribution of signatures characteristic to carotene at 1520 cm^{-1}. These four maps fill the upper half of the image space. Considering that the tail structure experiences thickening towards the lower left corner, we may consider the second set of images to report only on the molecular species in the skin. Comparatively, the pattern of Raman signals in the first set of images is more regular (in the image space) because proteins are expected to be present regularly regardless of whether we sample in the epidermis or deeper below. It is necessary to note here that the Raman pattern in Fig. 5A does show a larger signal at the upper right half. We believe this is because carotene Raman scattering may contaminate the spectral contribution of phenylalanine: results of DFT studies (see Fig. 2F) indicate a β-carotene resonance at the higher frequency side of the phenylalanine characteristic signature (see Fig. 2D). This may explain the slight broadening of the Raman transition assigned to phenylalanine at 1001 cm^{-1}, as indicated in Fig. 2C.

Conclusions

Using labelling free Raman micro-spectroscopy and assisted with quantum chemistry we reviewed the distribution of molecular species in the blastopore lateral lip of Harrison stage 11 embryo as well as the eye ocular sample and caudal appendage sample of Harrison 33rd stage embryo of the albino axolotl. Proteins with a rich alpha-helical content dominate blastopore tissue. Due to the weak differentiation of the early developmental state, phospholipid, proteins and carotenoids demonstrated a similar distribution pattern in space. The ocular section of the embryo (at Harrison stage 33) demonstrates the lens hemisphere structure covered with an epidermal precursor of sclera. Under 532 nm exciting radiation, representative Raman spectra of the structure include a strong carotenoid contribution and weaker signals from phospholipid and proteins. Accounting for the intensity of the SH resonance, Raman diagnostics report on essentially the reduced state of the proteins. Darker fibrillar deposition at the surface tends to correlate with the presence of protein and anticorrelates with the presence of phospholipids. Spatially resolved sampling reveals the carotenoid content to follow phospholipid distributions. Raman microscopy of the 33rd Harrison embryo tail (caudal appendage sample) demonstrates that, overall, phospholipids dominate in the sampled region. The character of phospholipid resonances indicates that the alkyl chains are in a tight and relatively ordered lattice.[74] Raman diagnostics reveals the co-presence of collagen and proteins rich with alpha-helical structural component. As it the case of the ocular sample, carotenoids follow the phospholipid distribution, which dominate in skin mainly. Our results of protein sampling indicate that the embryonal tissue under the selected stage of development does allow amide I and III detection deep inside while using 532 nm radiation. While opaque, the blastopore and ocular region sample of the grown embryo do allow surface sampling, mostly. With respect to the organs under the indicated stage of development, this makes Raman microscopy helpful for regenerative studies upon external interventions. Trying to employ near infrared radiation in the spectral region of tissue optical transparency may allow a better extended three-dimensional sampling capacity. The results provide the basis for quantitative analysis using theory approaches reported previously.[18,77] We believe this contribution will be helpful for those involved in planning experiments to combine biochemistry, emission and Raman microscopy to research axolotl tissue regeneration mechanisms.

Data availability

The data supporting this article have been included as part of the ESI.†

Conflicts of interest

There are no conflicts of interest to declare.

Acknowledgements

Funding from AFOSR FA9550-20-1-0206 and FA9550-24-1-0274 is gratefully acknowledged. The authors are thankful to Dr Fernando R. Clemente (Gaussian Inc., Wallingford, USA) for stimulating discussions. The computations in this paper were run on the Cannon cluster supported by the Faculty of Arts and Sciences division, Research Computing Group at Harvard University. Since 2021, VVV is a self-funded researcher living in Russia on savings collected during the USA Air Force Research program at Nottingham Trent University, 2016–2020.

References

1 H. M. Smith, *BioScience*, 1969, **19**, 593–598.
2 R. G. Harrison, *Organization and Development of the Embryo*, Yale Univ. Press, New Haven, CT, 1969, pp. 44–66.
3 G. M. Schreckenberg and A. G. Jacobson, *Dev. Biol.*, 1975, **42**, 391–400.
4 R. G. Harrison, *Proc. Natl. Acad. Sci. U. S. A.*, 1924, **10**, 69–74.
5 R. G. Harrison, *Dev. Genes Evol.*, 1929, **120**, 1–55.
6 B. M. Carlson, *Principles of regenerative biology*, Elsevier Academic Press, Amsterdam, Burlington, MA, 2007.
7 B. Galliot and L. Ghila, *Mol. Reprod. Dev.*, 2010, **77**, 837–855.
8 A. L. Mescher and A. W. Neff, *Adv. Biochem. Eng./Biotechnol.*, 2005, **93**, 39–66.
9 J. W. Godwin and J. P. Brockes, *J. Anat.*, 2006, **209**, 423–432.

10 F. Song, B. Li and D. L. Stocum, *Organogenesis*, 2010, **6**, 141–150.
11 K. Tamura, S. Ohgo and H. Yokoyama, *Dev., Growth Differ.*, 2010, **52**, 89–99.
12 C. McCusker, S. V. Bryant and D. M. Gardiner, *Regeneration*, 2015, **2**, 54–71.
13 D. L. Stocum and N. Rao, *Principles of regenerative medicine*, Elsevier Academic Press, 2011, pp. 67–86.
14 D. M. Bryant, *et al.*, *Cell Rep.*, 2017, **18**, 762–776.
15 A. Polikarpova, A. Ellinghaus, O. Schmidt-Bleek, L. Grosser, C. H. Bucher, G. N. Duda, E. M. Tanaka and K. Schmidt-Bleek, *npj Regener. Med.*, 2022, **7**, 35.
16 O. Uckermann, J. Hirsch, R. Galli, J. Bendig, R. Later, E. Koch, G. Schackert, G. Steiner, E. Tanaka and M. Kirsch, *Sci. Rep.*, 2019, **9**, 12641.
17 F. Vernuccio, E. Broggio, S. Sorrentino, A. Bresci, R. Junjuri, M. Ventura, R. Vanna, T. Bocklitz, M. Bregonzio, G. Cerullo, H. Rigneault and D. Polli, *Sci. Rep.*, 2024, **14**, 23903.
18 V. V. Volkov, T. J. Blundell, S. Argent and C. C. Perry, *Dalton Trans.*, 2023, **52**, 7249–7257.
19 G. Rusciano, G. Pesce, M. Salemme, L. Selvaggi, C. Vaccaro, A. Sasso and R. Carotenuto, *Methods*, 2010, **51**, 27–36.
20 L. Bogliolo, S. Ledda, P. Innocenzi, F. Ariu, D. Bebbere, I. Rosati, G. G. Leoni and M. Piccinini, *Cryobiology*, 2012, **64**, 267–272.
21 M. Ishigaki, K. Hashimoto and H. Sato, *et al.*, *Sci. Rep.*, 2017, **7**, 43942.
22 E. Perevedentseva, A. Krivokharchenko and A. V. Karmenyan, *et al.*, *Sci. Rep.*, 2019, **9**, 6636.
23 G. Rusciano, C. De Canditiis, G. Zito, M. Rubessa, M. S. Roca, R. Carotenuto, A. Sasso and B. Gasparrini, *PLoS One*, 2017, **12**, e0177677.
24 V. Olmos, M. Marro, P. Loza-Alvarez, D. Raldúa, E. Prats, B. Piña, R. Tauler and A. de Juan, *Talanta*, 2019, **194**, 390–398.
25 H. Høgset, C. C. Horgan, J. P. K. Armstrong, M. S. Bergholt, V. Torraca, Q. Chen, T. J. Keane, L. Bugeon, M. J. Dallman, S. Mostowy and M. M. Stevens, *Nat. Commun.*, 2020, **11**, 6172.
26 R. Manoharan, Y. Wang and M. S. Feld, *Spectrochim. Acta, Part A*, 1996, **52**, 215–249.
27 W. Müller, M. Kielhorn, M. Schmitt, J. Popp and R. Heintzmann, *Optica*, 2016, **3**, 452–457.
28 J. Li, P. Yan, Y. Li, M. Han, Q. Zeng, J. Li, Z. Yu, D. Zhang and X. Chen, *Front. Chem.*, 2023, **11**, 1211121.
29 G. Pezzotti, W. Zhu, Y. Terai, E. Marin, F. Boschetto, K. Kawamoto and K. Itaka, *Mater. Today Bio.*, 2022, **13**, 100210.
30 M. M. Casco-Robles, K. Yasuda, K. Yahata, F. Maruo and C. Chiba, *Biomedicines*, 2021, **9**, 1426.
31 National Research Council, *Guide for the care and use of laboratory animals*, National Academies Press, Washington, DC, 2011.
32 V. V. Volkov, G. J. Hickman, A. Sola-Rabada and C. C. Perry, *Front. Plant Sci.*, 2019, **10**, 210.
33 R. C. Spiker and I. W. Levin, *Biochim. Biophys. Acta*, 1976, **455**, 560–575.
34 R. C. Spiker and I. W. Levin, *Biochim. Biophys. Acta*, 1976, **433**, 457–468.
35 V. V. Volkov, R. Chelli, W. Zhuang, F. Nuti, Y. Takaoka, A. M. Papini, S. Mukamel and R. Righini, *Proc. Natl. Acad. Sci. U. S. A.*, 2007, **104**, 15323–15327.
36 P. Michaely, D. R. Tomchick, M. Machius and R. G. W. Anderson, *EMBO J.*, 2002, **21**, 6387–6396.
37 P. Bazylewski, R. Divigalpitiya and G. Fanchini, *RSC Adv.*, 2017, **7**, 2964.
38 M. Obika, *Dev. Biol.*, 1963, **6**, 99–112.
39 J. T. Bagnara and M. E. Hadley, *Chromatophores and Color Change*, Prentice-Hall, Englewood, New Jersey, 1973.
40 S. K. Frost, L. G. Epp and S. J. Robinson, *J. Embryol. Exp. Morphol.*, 1984, **81**, 105–125.
41 R. R. Humphrey, *J. Hered.*, 1967, **58**, 95–101.
42 S. K. Frost, L. G. Epp and S. J. Robinson, *J. Embryol. Exp. Morphol.*, 1986, **92**, 255–268.
43 G. M. Lowe, A. J. Young and D. M. Phillip, *Carotenoids in Health and Disease*, Marcel Dekker, New York, 2004, pp. 105–126.
44 H. I. Krinsky and S. M. Deneke, *J. Natl. Cancer Inst.*, 1982, **69**, 205–210.
45 H. Stransky and I. Schulze, *J. Comp. Physiol.*, 1977, **115**, 265–277.
46 J. K. Tyczkowski, J. L. Schaeffer, C. Parkhurst and P. B. Hamilton, *Poult. Sci.*, 1986, **65**, 2135–2141.
47 P. Bhosale, B. Serban, D. Y. Zhao and P. S. Bernstein, *Biochemistry*, 2007, **46**, 9050–9057.
48 A. D. Becke, *Phys. Rev. A:At., Mol., Opt. Phys.*, 1988, **38**, 3098–3100.
49 C. Lee, W. Yang and R. G. Parr, *Phys. Rev. B: Condens. Matter Mater. Phys.*, 1988, **37**, 785–789.
50 M. J. Frisch, G. W. Trucks, H. B. Schlegel, G. E. Scuseria, M. A. Robb, J. R. Cheeseman, G. Scalmani *et al.*, *Gaussian development version*, Revision h, 2010, **vol. 1**.
51 J. F. Meckel, System der Vergleichenden Anatomie, 7 Bde. RengerscheBuchhandlung, Halle, 1821.
52 E. R. A. Serres, Anatomie comparée du cerveau dans les quatre classes des animaux vertébrés, Paris, 1824.
53 B. P. Gaber and W. L. Peticolas, *Biochim. Biophys. Acta, Biomembr.*, 1977, **465**, 260–274.
54 B. G. Frushour and J. L. Koenig, *Biopolymers*, 1975, **14**, 379–391.
55 R. Snyder, S. Hsu and S. Krimm, *Spectrochim. Acta, Part A*, 1978, **34**, 395–406.
56 L. Norlen, *J. Invest. Dermatol.*, 2001, **117**, 830–836.
57 M. Ishigaki, K. Hashimoto, H. Sato and Y. Ozaki, *Sci. Rep.*, 2017, **7**, 43942.
58 M. Rhinn and P. Dolle, *Development*, 2012, **139**, 843–858.
59 R. Cuny and G. M. Malacinski, *J. Embryol. Exp. Morphol.*, 1986, **96**, 151–170.
60 K. G. Brown, W. L. Peticolos and E. Brown, *Res. Commun.*, 1973, **54**, 358–364.
61 Y. Koyama, *Carotenoids, vol. 1B, Spectroscopy*, Birkhäuser, Basel, 1995, pp. 135–146.
62 P. S. Bernstein and W. Gellermann, *Carotenoids in Health and Disease*, Marcel Dekker, New York, 2004, pp. 73–104.
63 L. C. Chen, L. Sly, C. S. Jones, R. De Tarone and L. M. Luca, *Carcinogenesis*, 1993, **14**, 713–717.
64 N.-T. Yu and E. J. East, *J. Biol. Chem.*, 1975, **250**, 2196–2202.

65 P. F. Kador, H. N. Fukui, S. Fukushi, H. M. Lernigan and J. H. Kinoshita, *Exp. Eye Res.*, 1980, **30**, 59.
66 Y. Ozaki, A. Mizuno, K. Itoh, M. Yoshiura, T. Iwamoto and K. Iriyama, *Biochemistry*, 1983, **22**, 6254.
67 P. Bazylewski, R. Divigalpitiya and G. Fanchini, *RSC Adv.*, 2017, **7**, 2964.
68 E. J. East, R. C. C. Chang and N.-T. Yu, *J. Biol. Chem.*, 1978, **253**, 1436–1441.
69 J. F. R. Kuck Jr., N.-T. Yu and C. C. Askren, *Exp. Eye Res.*, 1982, **34**, 23–37.
70 J. Pande, M. J. McDermott, R. Callender and A. Spector, *Arch. Biochem. Biophys.*, 1989, **269**, 250–255.
71 M. S. Jarial, *J. Anat.*, 1989, **167**, 95–102.
72 S. Gerling, J. D'Haese and H. Greven, *Vertebr. Zool.*, 2012, **62**, 97–111.
73 A. W. Seifert, J. R. Monaghan, S. R. Voss and M. Maden, *PLoS One*, 2012, **7**, e32875.
74 G. J. Fisher, J. Varani and J. J. Voorhees, *Arch. Dermatol.*, 2008, **144**, 666–672.
75 H. Akutsu, *Biochemistry*, 1981, **20**, 7359–7366.
76 E. Ly, O. Piot, A. Durlach, P. Bernard and M. Manfait, *Appl. Spectrosc.*, 2008, **62**, 1088–1094.
77 V. Volkov and C. C. Perry, *Microsc. Microanal.*, 2016, **22**, 1128–1145.

